ADVANCED FUNCTIONAL MATERIALS
www.afm-journal.de

2D Bismuthene as a Functional Interlayer between $BiVO_4$ and NiFeOOH for Enhanced Oxygen-Evolution Photoanodes

*Junyi Cui, Matyas Daboczi, Miriam Regue, Yi-Chun Chin, Katia Pagano, Jifang Zhang, Mark A. Isaacs, Gwilherm Kerherve, Aris Mornto, James West, Sixto Gimenez, Ji-Seon Kim, and Salvador Eslava**

$BiVO_4$ has attracted wide attention for oxygen-evolution photoanodes in water-splitting photoelectrochemical devices. However, its performance is hampered by electron-hole recombination at surface states. Herein, partially oxidized two-dimensional (2D) bismuthene is developed as an effective, stable, functional interlayer between $BiVO_4$ and the archetypal NiFeOOH co-catalyst. Comprehensive (photo)electrochemical and surface photovoltage characterizations show that NiFeOOH can effectively increase the lifetime of photogenerated holes by passivating hole trap states of $BiVO_4$; however, it is limited in influencing electron trap states related to oxygen vacancies (V_O). Loading bismuthene on $BiVO_4$ photoanodes increases the density of V_O that are beneficial for the oxygen evolution reaction via the formation of oxy/hydroxyl-based water oxidation intermediates at the surface. Moreover, bismuthene increases interfacial band bending and fills the V_O-related electron traps, leading to more efficient charge extraction. With the synergistic interaction of bismuthene and NiFeOOH on $BiVO_4$, this composite photoanode achieves a 5.8-fold increase in photocurrent compared to bare $BiVO_4$ reaching a stable 3.4 (±0.2) mA cm^{-2} at a low bias of +0.8 V_{RHE} or 4.7(±0.2) mA cm^{-2} at +1.23 V_{RHE}. The use of 2D bismuthene as functional interlayer provides a new strategy to enhance the performance of photoanodes.

1. Introduction

Photoelectrochemical (PEC) water splitting is a promising technique for producing hydrogen from water and sunlight, providing a sustainable alternative to the conventional production of hydrogen via methane reforming.[1] Achieving its full potential requires developing photoanodes that efficiently absorb solar light and drive the kinetically-demanding oxygen evolution reaction (OER). Among the numerous light absorber candidates such as Si,[2] WO_3,[3] TiO_2,[4,5] and α-Fe_2O_3,[6] $BiVO_4$ has attracted considerable attention. $BiVO_4$ has a relatively narrow bandgap of ≈2.4 eV allowing effective solar light absorption, n-type character enabling suitable band bending for charge transfer to aqueous electrolytes, and a thermodynamically suitable valence band edge at approximately +2.5 V versus the reversible hydrogen electrode (V_{RHE}) deep enough for OER.[7] However, $BiVO_4$ has an intrinsically low charge carrier

J. Cui, M. Daboczi, M. Regue, A. Mornto, J. West, S. Eslava
Department of Chemical Engineering
Imperial College London
London SW7 2AZ, UK
E-mail: s.eslava@imperial.ac.uk

Y.-C. Chin, K. Pagano, J.-S. Kim
Department of Physics
Imperial College London
London SW7 2AZ, UK

The ORCID identification number(s) for the author(s) of this article can be found under https://doi.org/10.1002/adfm.202207136.

DOI: 10.1002/adfm.202207136

J. Zhang
School of Physical Science and Technology
Shanghai Tech University
Shanghai 201210, P. R. China

M. A. Isaacs
Department of Chemistry
University College London
London WC1H 0AJ, UK

G. Kerherve
Department of Materials
Imperial College London
London SW7 2AZ, UK

S. Gimenez
Institute of Advanced Materials (INAM)
Universitat Jaume I
Castelló 12006, Spain

mobility of 0.04 $cm^2\ V^{-1}\ s^{-1}$, poor catalytic ability for OER on its surface, and limited stability.[8,9] To overcome these limitations and thereby boost the performance of $BiVO_4$, several strategies—including doping, facet engineering, nano structuring, and co-catalyst loading—have been developed.[10] Co-catalysts loaded on $BiVO_4$ are expected to boost the performance of the resulting photoanodes by adopting one or more different roles: 1) enhancing OER kinetics; 2) improving interfacial energetics; 3) storing and transferring holes for OER, and/or 4) increasing stability.[11]

The search for co-catalyst candidates has often been restricted to oxygen evolution catalysts (OECs) used in water electrolysis, such as cobalt phosphates (Co-Pi).[11] However, functional interlayers between the light absorber and the OEC, which have been far less investigated, may result in unique synergies to further harness the benefits of the OEC. One such example is superhydrophilic graphdiyne (GDY), which has been reported to transfer charges between $BiVO_4$ and a CoAl (CO_3^{2-}) layered double hydroxide electrocatalyst.[12] Other materials such as polyaniline,[13] ferrihydrite (Fh),[14] and surface hydroxyl groups[15] have also been reported to improve hole transfer between semiconductors and OECs. Recently, Park et al. employed four layers of exfoliated 2D black phosphorene,[16,17] between $BiVO_4$ and NiOOH to assist interfacial charge injection, and found that the *p*-type character of black phosphorene helps boost hole extraction, therefore increasing photocurrent.

Bismuthene is a promising 2D VA-group material with useful properties for photoelectrochemical devices such as a high carrier mobility of ≈384 $cm^2\ V^{-1}\ s^{-1}$, spin-orbit interaction, and general environmental friendliness.[18–20] It was first synthesized under ultra-high vacuum,[21] but alternative methods have also been reported such as liquid-phase exfoliation, electrochemical exfoliation, and mechanical exfoliation.[17] Most recently, Yang et al. reported a scalable wet-chemical synthetic method to achieve free-standing bismuthene.[18] Bismuthene demonstrated excellent performance in electrochemical CO_2 reduction cells,[18] ultrafast fiber lasers,[22] and potassium-ion batteries.[23]

Herein, we present partially oxidized bismuthene as a functional interlayer between $BiVO_4$ and an archetypal electrocatalyst, NiFeOOH. The $BiVO_4$/Bi/NiFeOOH composite photoanode generates a high photocurrent of 3.4 (±0.2) mA cm^{-2} at a low bias of +0.8 V_{RHE}, approximately six times higher than bare $BiVO_4$ photoanodes. An extended physico-chemical and (photo)electrochemical characterization shows the complementary roles of bismuthene and NiFeOOH. We find that using both NiFeOOH and bismuthene can simultaneously passivate hole and electron traps in $BiVO_4$. NiFeOOH reduces the density of hole traps and, hence, surface recombination. Partially oxidized bismuthene increases the density of oxygen vacancies at the surface of $BiVO_4$, which are known to act as adsorption sites of oxy/hydroxyl species needed for water oxidation. Simultaneously, bismuthene fills these oxygen vacancy related surface states and by that passivates them as electron traps. Consequently, the addition of bismuthene increases the *n*-type character of $BiVO_4$ as well as the interfacial band bending and thereby enhances charge separation and transfer. This work highlights the importance of functional interlayers for photoelectrodes and reveals the great potential of 2D bismuthene in photoelectrodes.

2. Results and Discussion

2.1. Synthesis and Characterization of $BiVO_4$/Bi/NiFeOOH Photoanodes

We synthesized $BiVO_4$ photoanodes and subsequently loaded bismuthene and NiFeOOH, as illustrated in **Figure 1**a,b. $BiVO_4$ was prepared on fluorine-doped tin oxide (FTO) coated glass using a BiOI-assisted method.[24] The $BiVO_4$ composition and crystallographic structure were characterized by Raman spectroscopy and X-ray diffraction (XRD). Raman bands are observed at 211, 326, 366, 718, and 827 cm^{-1}, corresponding to those of clinobisvanite $BiVO_4$ (RRUFF ID R070401, Figure S1, Supporting Information). XRD patterns show that the $BiVO_4$ crystal system is monoclinic, which is the most active phase for photocatalysis[25] (JCPDS 00-014-0688, Figure S2, Supporting Information). The morphology of $BiVO_4$ was analyzed by scanning and high-resolution transmission electron microscopy (SEM and HR-TEM). SEM micrographs show that the prepared $BiVO_4$ film is highly porous, ≈700 nm thick, and has a worm-like morphology with features ≈200 nm in size (Figure 1c,d). TEM micrographs show a highly rough $BiVO_4$ surface with small crystalline dots (Figure 1e; Figure S3, Supporting Information). Lattice features observed by HR-TEM also confirm the presence of $BiVO_4$ (Figure 1g; Figure S3, Supporting Information). These porous $BiVO_4$ films provide a large surface area for the loading of co-catalysts.

2D bismuthene was chemically synthesized by reducing $BiCl_3$ with $NaBH_4$.[18] An XRD pattern of the as-filtered and as-washed bismuthene exhibits the characteristic pattern of bismuth metal, indicating the successful reduction of $BiCl_3$ (Figure S4a, Supporting Information). The stability of the synthesized bismuthene was investigated by annealing at 200 °C in air for 1 h. After annealing, the characteristic XRD pattern of bismuth metal is kept, with only a small presence of oxidized phases, evidencing its good air stability. Raman spectroscopy also confirms the successful reduction of $BiCl_3$ to bismuthene (Figure S4b, Supporting Information). Raman bands at 88.5 and 122.0 cm^{-1} are assigned to E_g (in-plane mode) and A_{1g} (out-of-plane mode) vibration modes of Bi atoms, respectively.[26–29] Compared with the Raman bands of pure bismuth metal, typically narrow bands at 70.0 and 97.0 cm^{-1},[30] a shift to higher wavenumbers and a pronounced broadening indicate the decrease of long-range ordering herein assigned to the 2D shape.[31] The blue shift of the A_{1g} vibration mode is larger than that of the E_g one, and the E_g vibration mode shows a relatively smaller intensity. These shifts are also assigned to the 2D structure and to a layer number effect.[32] There is an additional band at 306.0 cm^{-1}, which does not belong to bismuthene or bismuth metal, and indicates that the bismuthene is partially oxidized. Since optical microscopy shows a change of color of the sample upon Raman spectroscopy measurement, part of this oxidation must occur during the laser irradiation (Figure S4b inset, Supporting Information).[33]

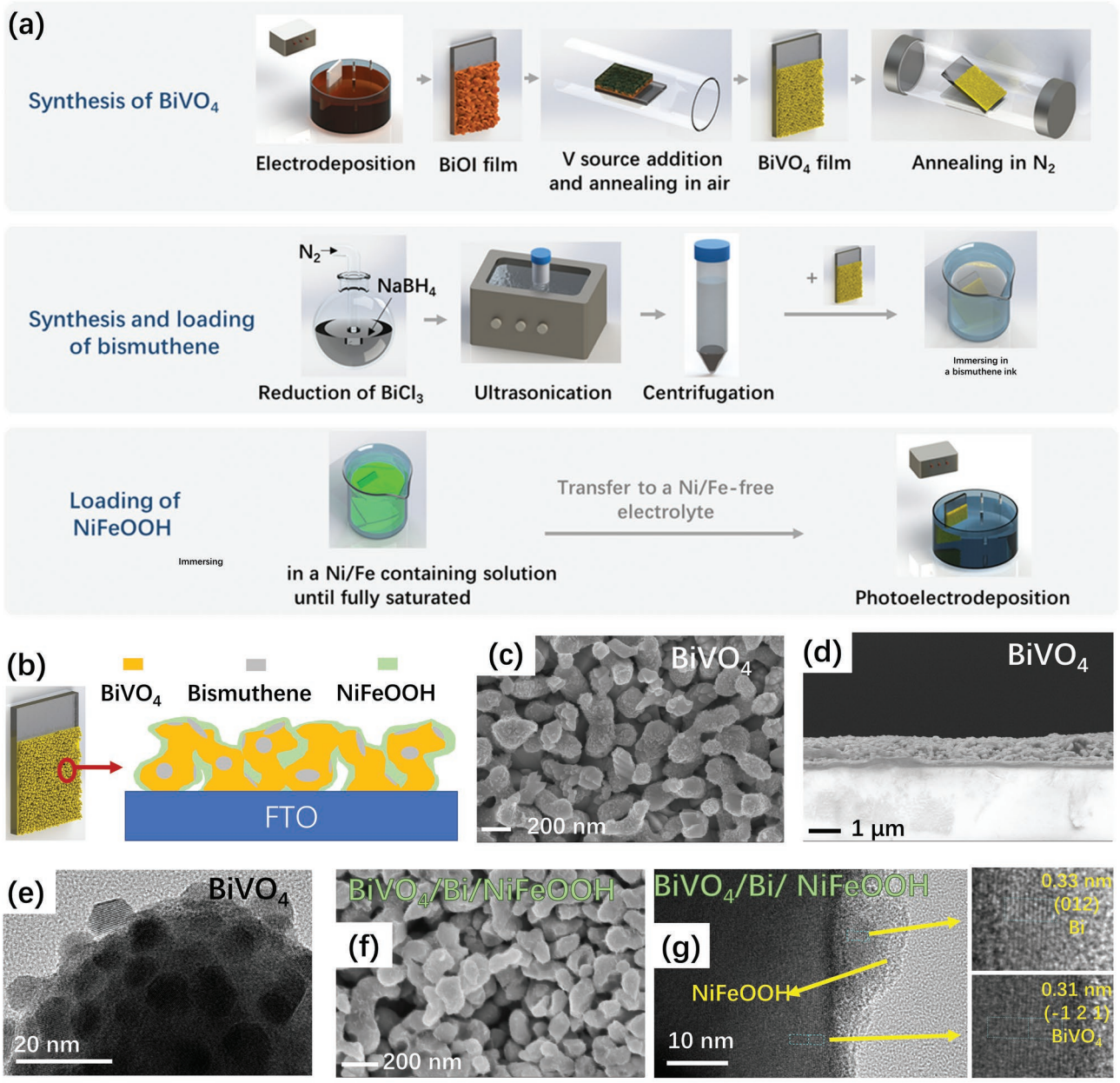

Figure 1. a) Schematic diagram illustrating the fabrication steps of $BiVO_4$/Bi/NiFeOOH composite photoanodes. b) Schematic diagram illustrating the composite photoanode. SEM micrographs of $BiVO_4$ c) top surface and d) cross-section, and f) $BiVO_4$/Bi/NiFeOOH top surface. HR-TEM micrographs of e) $BiVO_4$ and g) $BiVO_4$/Bi/NiFeOOH, including lattice fringe spacing calculation ($BiVO_4$: JCPDS 00-014-0688; Bi: JCPDS 00-044-1246). More enlarged micrographs are displayed in Figure S3 (Supporting Information).

The morphology and dimensions of the prepared bismuthene were inspected by TEM and atomic force microscopy AFM (Figure S5, Supporting Information). TEM micrographs show bismuthene has a 2D high aspect ratio, with a wide range of flake lateral sizes from ≈50 nm up to a few µm. AFM shows that the average thickness of the bismuthene flakes is 2.1–2.2 nm. Since the µm lateral size exceeds the typical pore size in the $BiVO_4$ films, we carried out ultrasonication and centrifugation, to exclude large flakes. After these steps, the collected bismuthene shows a thickness of 0.5–0.6 nm and an average lateral size of ≈50 nm (Figure S5, Supporting Information). More characterization of bismuthene, including Mott–Schottky plot, valence-band XPS, UV-vis spectroscopy and photographs can be found in Figure S6 (Supporting Information).

X-ray photoelectron spectroscopy (XPS) was used to further characterize the prepared bismuthene. An XPS Bi 4*f* spectrum of bismuthene shows two doublets, located at 156.3 and 158.4 eV for Bi $4f_{7/2}$ (Figure S4c, Supporting Information). The peaks at 156.3 and 158.4 eV are assigned to metallic Bi (0) and Bi—O, respectively,[34] confirming the partial oxidation of bismuthene. Partial oxidation of bismuthene has been proposed

to form a passivation layer that prevents further oxidation in air.[35] Interestingly, compared with bulk Bi metal (157.0 eV) and bismuth oxides (159.1 eV),[34] the two peaks of bismuthene both shift to lower binding energies. We assign this shift to electron enrichment on the edges of bismuthene.[36,37]

The collected bismuthene of reduced lateral size was loaded on the porous $BiVO_4$ photoanodes by suspending the bismuthene in ethanol and immersing the photoanodes for 2 h. We note that bismuthene easily adsorbs on different surfaces such as $BiVO_4$ or glass, probably by electrostatic forces. NiFeOOH was prepared on the surface of the photoanodes with and without bismuthene by photoelectrochemical deposition.[24] HR-SEM micrographs do not reveal significant differences with the loading of bismuthene and NiFeOOH due to their small dimensions, but energy-dispersive X-ray spectroscopy (EDS) mapping clearly shows a uniform distribution of Fe and Ni elements (Figure S7, Supporting Information). HR-TEM micrographs confirm that both bismuthene and NiFeOOH layers are successfully loaded (Figure 1g; Figure S3, Supporting Information). The lattice fringe spacing of bismuthene and $BiVO_4$ is significantly different (values 0.31 ± 0.004 vs 0.33 ± 0.004 nm), which allows confirming the presence of bismuthene. Bismuthene is found on the surface of $BiVO_4$ in $BiVO_4$/Bi samples, and between $BiVO_4$ and NiFeOOH in $BiVO_4$/Bi/NiFeOOH samples. A good distribution of bismuthene on the $BiVO_4$ surface is shown, even in narrow $BiVO_4$ valleys (Figure S3d, Supporting Information). The NiFeOOH layer is ≈10 nm thick and amorphous. XRD patterns of the prepared photoanodes with and without bismuthene and NiFeOOH are similar, in agreement with these layers being very thin compared to $BiVO_4$ (Figure S2, Supporting Information). Similarly, $BiVO_4$ Raman bands do not show any significant shift (Figure S1, Supporting Information).

Further evidence of bismuthene and NiFeOOH loading is found by XPS. **Figure 2**a shows Bi*4f* XPS peaks at 158.9 and 164.3 eV assigned to Bi $4f_{7/2}$ and Bi $4f_{5/2}$ bonded to O, respectively.[38] The peak areas of the bismuthene-containing photoanodes are larger than those of the bismuthene-free ones, indicating the successful loading of bismuthene on $BiVO_4$ surfaces (Figure S8a (Supporting Information), normalized with the areas of V $2p_{3/2}$). The presence of a peak at 157.3 eV in $BiVO_4$/Bi is assigned to Bi(0) and confirms the successful loading of bismuthene on $BiVO_4$ surfaces. This Bi(0) peak is absent in $BiVO_4$/Bi/NiFeOOH, probably due to the covering of surfaces with the 10 nm of NiFeOOH. However, signal broadening at the high binding energy side at ≈160.5 and 165.5 eV is clearly observed in both samples with bismuthene (Figure 2a; Figure S8, Supporting Information). This asymmetric signal broadening is not seen in the XPS spectrum of pure bismuthene (Figure S4c, Supporting Information); therefore, we assign it to Bi atoms in the $BiVO_4$. Since the bismuthene layer is only 0.6 nm, we first exclude the possibility of inelastic scattering of Bi *4f* photoelectrons from the bismuthene layer because the inelastic mean free path, normally several nm,[39] is much larger than the layer thickness of bismuthene. Moreover, this additional signal is not observed on NiFeOOH-containing photoanodes, further indicating it is caused by an electronic perturbation, rather than inelastic scattering. A similar signal broadening at the high binding energy side of Bi *4f* in bismuth strontium calcium copper oxide has been reported as a result of the release of O atoms.[40] Hence, we relate this additional signal broadening in photoanodes containing bismuthene to changes of the Bi environment by the presence of oxygen vacancies.

Other interesting features are observed in the O 1s and V 2p XPS when bismuthene is added. Figure 2b shows the O 1s peaks at 529.6 and 531.5 eV that are assigned to lattice O and

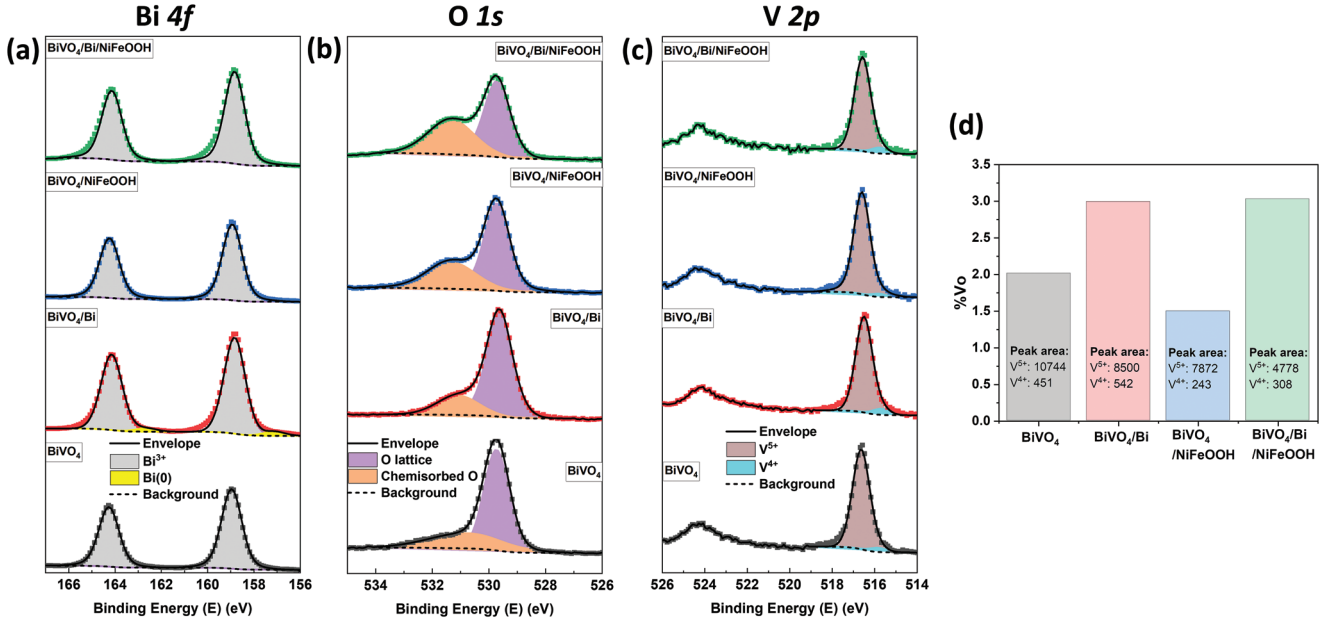

Figure 2. XPS spectra of $BiVO_4$-based photoanodes: a) Bi 4f; b) O 1s; and c) V 2p. Scattered points correspond to raw data acquired in the measurements and solid lines to the fitted values. d) Calculated atomic percentages of V_O from the relative area of V^{4+} and V^{5+}. Excess electrons from each oxygen vacancy site give rise to two equivalents of V^{4+}species. Reproducibility of the analysis for different series of samples is confirmed in Figure S10 (Supporting Information).

chemisorbed O (i.e., −OH and −CO group), respectively. With the addition of NiFeOOH, there is a rise in the chemisorbed O peak, which we assign to the presence of NiFeOOH itself. With the addition of bismuthene, there is also an increase of the chemisorbed O peaks, which could be related to the increased density of V_O but also to a larger amount of adsorbed carbon oxides.[41,42] Figure 2c shows the V 2p peaks at 516.5 and 515.7 eV, that are assigned to the $2p_{3/2}$ of V^{5+} and V^{4+}, respectively.[38] Compared to the complex chemisorbed O peak, the V^{4+} peak is clearly caused by V_O because V_O formation leads to the localization of electrons on the neighboring *V* sites, reducing them from V^{5+} to V^{4+}.[43] After loading bismuthene, atomic percentages of V^{4+} increased and the calculated V_O also increased significantly from ≈1.5 or 2% to ≈3%, confirming that loading of bismuthene increases the surface V_O density (Figure 2d). The increased amount of V_O, originating from the interaction with bismuthene, probably occurs because oxygen vacancies can form at significantly lower cost when a metal is in contact with an oxide surface.[44] Moreover, mixing a metal oxide with a reductant can remove lattice O.[45–47] Since bismuthene is in low valence state, it probably attracts the surface lattice O to create V_O. Finally, Fe 2*p* XPS peaks are observed in photoanodes containing NiFeOOH, indicating its successful loading (Figure S9, Supporting Information). The position of the Fe $2p_{3/2}$ satellite is found at binding energy ≈720 eV which is characteristic of Fe^{3+} and further confirms the presence of NiFeOOH at the surface.

2.2. PEC Water Oxidation

The PEC performance of each $BiVO_4$ photoanode, prepared with or without bismuthene and/or NiFeOOH, was evaluated by measuring current-voltage curves under chopped simulated sunlight (Xe source, AM 1.5G filter, 100 mW cm^{-2}), using a 1 M potassium borate buffer electrolyte (KB, pH 9) in a three-electrode electrochemical cell. The bare $BiVO_4$ photoanode registers a photocurrent density of 2.0(±0.1) mA cm^{-2} at +1.23 V_{RHE}, which almost doubles the commonly reported values for $BiVO_4$ photoanodes (**Figure 3**a).[48–51] Notably, the relatively small size of the film features ≈100 nm radius, only slightly larger than the $BiVO_4$ carrier diffusion length of 70 nm [52] is expected to keep a low bulk recombination. However, at a low bias of +0.8 V_{RHE}, the bare $BiVO_4$ photoanode generates only 0.7(±0.1) mA cm^{-2} photocurrent density with a high onset potential of +0.63 V_{RHE} (conservatively defined by linear extrapolation using the maximum slope of the current rise under illumination). Upon the addition of bismuthene, the photocurrent density increases, especially at a higher bias, reaching 1.00(±0.02) mA cm^{-2} at +0.8 V_{RHE} and 2.7 (±0.1) mA cm^{-2} at +1.23 V_{RHE} with a cathodic shift of the onset potential to +0.57 V_{RHE}. Upon the addition of NiFeOOH, the photocurrent density at +1.23 V_{RHE} further increases up to a remarkable 3.9 (±0.2) and 4.7 (±0.2) mA cm^2 for the $BiVO_4$/NiFeOOH and $BiVO_4$/Bi/NiFeOOH photoanodes, respectively; at a lower bias of +0.8 V_{RHE}, $BiVO_4$/NiFeOOH and $BiVO_4$/Bi/NiFeOOH achieve 5.1- and 5.8-fold

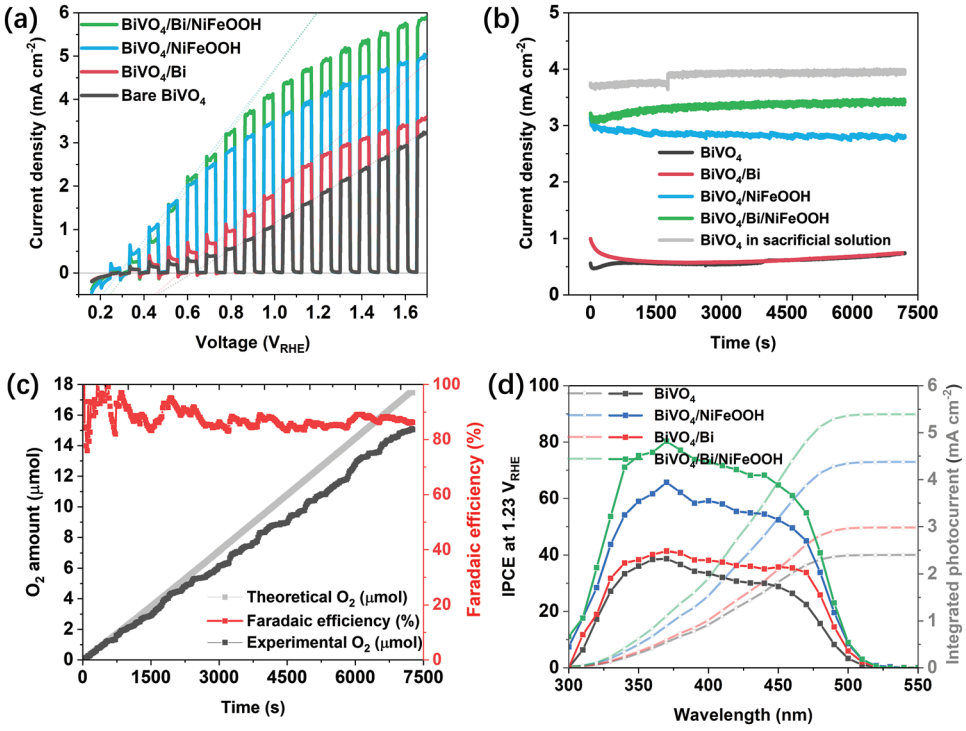

Figure 3. a) Photocurrent density-voltage curves of $BiVO_4$ photoanodes with chopped illumination. Voltage scan rate: 10 mV s^{-1}. Reproducibility and error statistics are presented in Figure S11 (Supporting Information). b) Photocurrent density stability tests of photoanodes at +0.8 V_{RHE}. c) Amount of measured and theoretical oxygen evolution and calculated faradaic efficiency at +0.8 V_{RHE}. d) IPCE plots of $BiVO_4$ photoanodes at +1.23 V_{RHE} (left) and integrated photocurrents (right). All these measurements were carried out in a 1 M KB buffer solution with pH 9 under simulated sunlight (Xe source, AM 1.5G filter, 100 mW cm^{-2}) or under monochromatic light (Xe source and monochromator). Measurement in (b) with sacrificial agent was carried out by adding 0.5 M Na_2SO_3 to the same KB buffer solution.

increase in photocurrent density, respectively, compared to the reference $BiVO_4$ photoanode. Notably, the photocurrent density of $BiVO_4$/Bi/NiFeOOH reaches 3.4 (±0.2) mA cm^{-2} at +0.8 V_{RHE}, which is one of the highest reported values at such a low applied bias (Table S1, Supporting Information). Moreover, the onset potential of the composite photoanode significantly shifts down to +0.30 V_{RHE}. These trends are confirmed in other series of samples and their corresponding statistical analysis presented in Figure S11 (Supporting Information): both bismuthene and NiFeOOH cathodically shift the potential onset down to +0.30 V_{RHE} (i.e., the flat band potential) and increase photocurrents, reaching the best performance combining both.

To evaluate the stability of the photoelectrodes, chronoamperometry measurements were performed at +0.8 V_{RHE} (Figure 3b). The current density of the $BiVO_4$/Bi/NiFeOOH photoanode increases slightly over time to reach and maintain an average of 3.4 mA cm^{-2} at +0.8 V_{RHE} for 7200 s, indicating good stability. Longer-term stability measurements of 13 h confirm the trend and good stability (Figure S12, Supporting Information). In contrast, the $BiVO_4$/NiFeOOH sample, lacking the bismuthene functional layer, shows a decrease in photocurrent throughout the 7200 s from 3.0 to 2.7 mA cm^{-2} at the same bias. A more significant drop is observed for the $BiVO_4$/Bi photoanode, which cannot be assigned to degradation of the partially oxidized bismuthene since this is shown to be stable in repeated cyclic voltammetry (CV) measurements in oxidation environment up to +2 V_{RHE} (Figure S13a, Supporting Information). The stability of partially oxidized materials such as metals, metal phosphides and metal sulfides under OER conditions has been widely reported.[53–58] Then, the deterioration of the $BiVO_4$/Bi photocurrent density can be attributed to the anodic photocorrosion of $BiVO_4$ by accumulation of holes at the surface due to insufficient water oxidation capability.[24,59] The dissolution of $BiVO_4$ surface has been widely reported, with a $BiVO_4$ etching rate of ≈1 nm min^{-1}.[59,60] The dissolution likely results in detachment of bismuthene, which explains why both $BiVO_4$/Bi and bare $BiVO_4$ photoanodes reach the same photocurrent density after 1000 s of operation. Notably, the detachment of bismuthene is avoided when coated with the NiFeOOH layer, which then explains the improved stability of the $BiVO_4$/Bi/NiFeOOH composite photoanode. The photocurrent densities of all the photoanodes (except $BiVO_4$/NiFeOOH) show a slow, continuous increase during the stability test (after the initial drop when present), assigned to photocharging of $BiVO_4$.[24,61,62] Some articles assigned this improvement to a change of surface states that reduces V^{5+} to V^{4+} or to formation of a new reversible layer.[62–64] $BiVO_4$/NiFeOOH does not show photocharging effect, but a slight decrease, which is perhaps because the NiFeOOH stores a large number of holes at the surface. Without the electron filling ability of bismuthene (shown later), these holes may prohibit the surface reduction of V^{5+} to V^{4+} or the formation of a new layer.

The amount of O_2 generated by the $BiVO_4$/Bi/NiFeOOH photoanode was measured in a gastight PEC cell using an O_2 sensor (Figure 3c). The O_2 evolution rate reached a remarkable 26.8 µmol cm^{-2} h^{-1} at +0.8 V_{RHE}, demonstrating the highly promising device performance. The average Faradaic efficiency for O_2 evolution was ≈85%, as calculated from the ratio of the measured amount of O_2 to the theoretical maximum amount—derived from the chronoamperometry curves. Possible reasons for not reaching 100% faradaic efficiency could be slight photocorrosion of $BiVO_4$, poor O_2 product desorption, and/or minor gas leaks.[65]

To further understand the effect of bismuthene and NiFeOOH on the photocurrent generation, the incident photon-to-current efficiency (IPCE) was measured at +0.8 and +1.23 V_{RHE} and different wavelengths (Figure S14, Supporting Information; Figure 3d). At +0.8 V_{RHE}, the $BiVO_4$/Bi photoanode reaches its highest IPCE value of 25% at 470 nm, which is significantly higher than the 14% for $BiVO_4$ at the same wavelength. The edges of the IPCE or UV–vis diffuse reflectance spectra (Figure S15, Supporting Information) remain the same after the deposition of bismuthene. Hence, the increased IPCE values with bismuthene at low incident photon energies (470–500 nm) indicate more efficient extraction of charge carriers. The IPCE spectra at +0.8 V_{RHE} of $BiVO_4$/NiFeOOH and $BiVO_4$/Bi/NiFeOOH reach maxima of 41% and 56%, respectively, confirming the improved charge carrier separation in the presence of bismuthene. The IPCE spectra measured at +1.23 V_{RHE} show the same trend as that at +0.8 V_{RHE} but with higher values, reaching a maximum IPCE value of 72% for the $BiVO_4$/Bi/NiFeOOH photoanode. Integrating the product of the IPCE curves and the photon intensity in the AM 1.5G solar spectrum allows to calculate photocurrent densities of 0.9, 1.3, 2.5, and 3.1 mA cm^{-2} at +0.8 V_{RHE} for $BiVO_4$, $BiVO_4$/Bi, $BiVO_4$/NiFeOOH, and $BiVO_4$/Bi/NiFeOOH, respectively (Figure S14, Supporting Information). These integrated photocurrent values for the AM 1.5G solar spectrum confirm the same trend and values (±5%) observed under simulated sunlight (Figure 3a).

Most studies on $BiVO_4$ focus on improvements of photocurrent at +1.23 V_{RHE}; however, a lower bias is more pertinent for the application of photoanodes that will be paired to a solar cell in series or to a photocathode to achieve enough photovoltage to drive redox reactions such as water splitting. Most importantly, $BiVO_4$ is unstable at a bias above +1.0 V_{RHE}, as it decomposes[24,66] into bismuth oxides (pH < 8: BiO^+, pH > 8: Bi_4O_7), and vanadium oxide (VO_4^-), as shown in its Pourbaix plot.[60,66,67] Table S1 (Supporting Information) presents photocurrents of recently developed modified $BiVO_4$ photoanodes coated with co-catalysts. The photocurrents obtained here with our $BiVO_4$/Bi/NiFeOOH achieve one of highest values in the literature, especially at the pertinent low bias of +0.8 V_{RHE}.

2.3. Role of Bismuthene and NiFeOOH on Interfacial Energetics

We employed a range of (photo)electrochemical and surface photovoltage techniques to gain a deeper understanding on the roles of bismuthene and NiFeOOH in the PEC performance enhancement of the $BiVO_4$ photoanodes. First, we carried out Kelvin probe measurements on the surface of the photoanodes in dark conditions (**Figure 4**a). These measurements show an (energetically) shallower Fermi level for the bismuthene-containing photoanodes, which is expected to generate an increased band bending at the interface with the electrolyte.[68] Second, open circuit potential (OCP) measurements in the dark and under saturated-illumination conditions (300 mW cm^{-2} simulated sunlight) were carried out (Figure 4b).

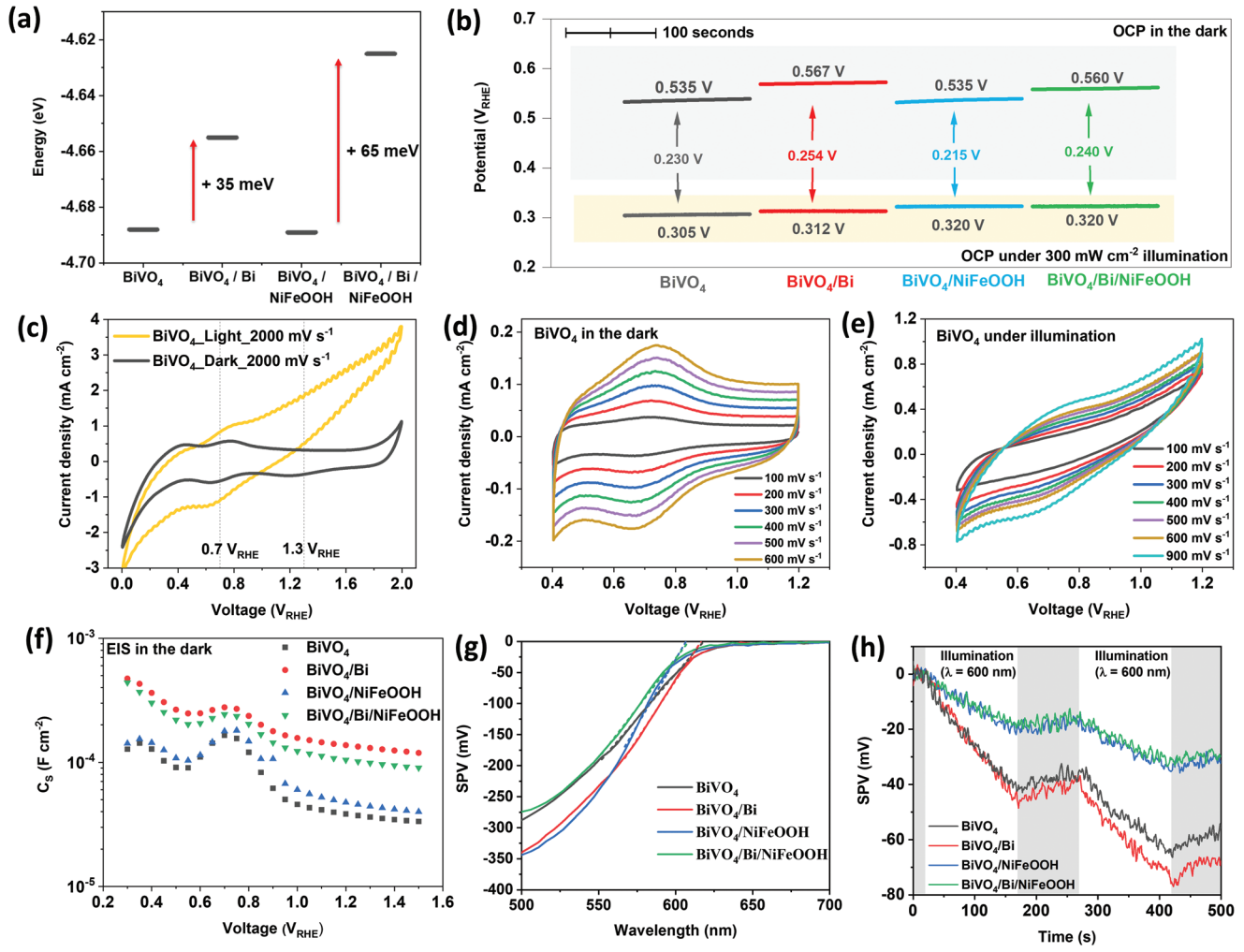

Figure 4. a) Fermi level of photoanodes measured by a vibrating tip Kelvin probe; b) OCP plots of photoanodes in the dark (grey background in graph) and under 300 mW cm^{-2} simulated sunlight (Xe source, AM 1.5G, yellow background in graph). 1000 mW cm^{-2} illumination results in the same values, but in an increase of noise and heating. c) CV plot of $BiVO_4$ at 2000 mV s^{-1} in the dark and under illumination. d) CV of $BiVO_4$ at various scan rates in the dark e) CV of $BiVO_4$ at various scan rates under illumination and corresponding linear relationship between peak current and (scan rate)$^{1/2}$; f) C_s versus voltage obtained from fitting EIS data in the dark. The change of C_s is related to the charge and discharge of surface states; g) Surface photovoltage of $BiVO_4$ photoanodes, showing an onset of the signal ≈600 nm. h) Negative SPV signal generated by two times repeated 100 s long sub-bandgap illumination ($\lambda = 600$ nm, indicated by white background color). All electrochemical measurements were done with N_2 purging to avoid any influence of ORR.

Photoanodes containing bismuthene show a significantly larger OCP change upon illumination, which confirms the presence of a larger interfacial electric field, i.e., a larger interfacial band bending.[69] Such an increased interfacial band bending favors hole transport toward the interface for water oxidation. The light-saturated OCP can also be used to determine the flat band potential.[70] All the photoanodes obtain very similar light-saturated OCP values of +0.31(±0.01) V_{RHE}, hence very similar flat band potential. The same flat band potential confirms that bismuthene and NiFeOOH do not alter the majority carrier density in the bulk of $BiVO_4$, but rather the equilibrium Fermi level of $BiVO_4$/bismuthene and interfacial band bending.

Interestingly, although the OCP should equilibrate with the water oxidation potential of +1.23 V_{RHE} in the dark, the values measured are far from that value (Figure 4b), indicating that the development of the space charge region (SCR) is hindered. One possible reason for this hindered SCR could be the microporous structure of the photoanode; however, this is unlikely as the width of the SCR is calculated to be ≈40 nm (considering the maximum observed band bending of 0.254 V_{RHE}, Note S1, Supporting Information), smaller than the $BiVO_4$ feature sizes that are in the 200 nm range. A more plausible explanation for the hindered SCR may therefore be Fermi level pinning caused by surface states.[71]

Surface states (ss) play an important role in PEC water oxidation, especially on metal oxide photoanodes, acting as recombination centers (r-ss) and reaction sites (i-ss).[11] Herein, we identify two different surface states on $BiVO_4$ by using CV and surface photovoltage (SPV) measurements. In the dark, the CV plots of $BiVO_4$ photoanodes display several cathodic and anodic peaks between +0.3 and +1.5 V_{RHE} (Figure 4c). The reduction peaks during the cathodic scan can be assigned to electron

trapping processes while the oxidation peaks during the anodic scan to electron detrapping.[72] At around +1.3 V_{RHE}, a reduction peak is observed, whereas the corresponding oxidation peak overlaps with the OER beyond +1.8 V_{RHE}, indicating that this is an irreversible surface trapping. Due to the overlap of the oxidation peak and the OER, the energetic position of these surface states cannot be obtained by CV; therefore, we carried out SPV measurements. The onset of SPV signal at ≈600 nm (Figure 4g) is at significantly lower energy compared to the bandgap of $BiVO_4$ (≈500 nm). This SPV signal at sub-bandgap illumination shows the presence of trap states at ≈0.4–0.5 eV above the valence band edge of $BiVO_4$, i.e., at +2.0–2.1 V_{RHE}. This high redox potential and the irreversible process show these surface states are recombination centers (r-ss). Their origin has been assigned elsewhere to VO^{2+}/VO_2^+ sites.[72,73]

By contrast, there is a pair of highly reversible redox peaks at around +0.7 V_{RHE}, which have previously been ascribed to the redox process of V^{4+}/V^{5+} involving the formation of V_O.[43,72] The peak current densities grow linearly with increasing scan rates (ν), which is characteristic of an adsorption-controlled pseudocapacitance process (Figure 4d; Figure S16, Supporting Information).[74] We attribute this fast trapping–detrapping pseudocapacitive process to the chemical adsorption-desorption of water molecules and its derivatives on V_O, resulting in oxy/hydroxyl-based water oxidation intermediates and enhanced photocurrents at this potential range (around +0.7 V_{RHE}).[72] This process becomes controlled by diffusion once illuminated, as evidenced by the peak current densities showing a linear relationship with $\nu^{1/2}$ (Figure 4e; Figure S17, Supporting Information).[74] Hence, different from a well-defined i-ss, the impact of these V_O is complex: V_O can act as adsorption sites helping OER but unfilled V_O can also trap electrons limiting electron extraction to the external circuit.[43]

The *n*-doped nature of $BiVO_4$, the existence of V^{4+} peak in the XPS spectra (Figure 2c), and the pinning of the Fermi level at the energy level of V_O (Figure 4b), discussed in previous sections, suggest the presence of numerous V_O on the surface. This is further verified by using electrochemical impedance spectroscopy (EIS). The capacitance related to surface states (C_s) shows a Gaussian distribution at +0.7 V_{RHE} (Figure 4f) corroborating the presence of surface states at this energy, which we linked to V_O and oxy/hydroxyl-based water oxidation intermediates. The EIS C_s plot for $BiVO_4$/NiFeOOH resembles that of the bare $BiVO_4$ photoanode, indicating that NiFeOOH has little impact on V_O, in the dark. However, we find that bismuthene increases the amount of V_O on the photoanode surface because higher capacitance values below +0.8 V_{RHE} are observed. The broader XPS signal at the high binding energy side of Bi *4f* (Figure S8, Supporting Information) and the larger atom percentage of V^{4+} (Figure 2c,d) further confirm a higher surface density of V_O in the presence of bismuthene.

In addition to increase the surface density of V_O, the presence of bismuthene is found to fill these V_O with electrons (i.e., as V^{4+}). Referring to the Kelvin probe measurements (Figure 4a), the Fermi level of the bismuthene-containing photoanodes is shallower than that of the bismuthene-free photoanodes. A shallower Fermi level means that bismuthene fills the V_O-related electronic trap states with electrons. As shown in Figure S6c (Supporting Information), the Fermi level of the partially oxidized bismuthene is shallower than that of $BiVO_4$. Electrons can flow from bismuthene to $BiVO_4$ to fill V_O until reaching an equilibrium. This charge redistribution could correspond to the broadened signal in Bi *4f* XPS spectra for bismuthene-containing photoanodes (Figure S8, Supporting Information). As shallow electron traps, these V_O are usually ionized (unoccupied) at the space charge region, which would trap photogenerated electrons from the conduction band.[43] However, being filled, these V_O cannot trap the photogenerated electrons; hence, bismuthene contributes toward a more efficient electron extraction into the external circuit.

To investigate the surface states (located at +2.0–2.1 V_{RHE}), assigned elsewhere to VO^{2+}/VO_2^+ sites,[72,73] and the influence of bismuthene and NiFeOOH on them, SPV measurements were conducted applying continuous 600 nm wavelength (sub-bandgap) monochromatic illumination at intervals (Figure 4h). SPV is defined here as the difference of surface potential measured under illumination (φ_{ill}) and under dark (φ_{dark}) conditions: SPV = $\varphi_{ill} - \varphi_{dark}$. The generation of a negative SPV signal under sub-bandgap (i.e., lower energy compared to the bandgap) illumination results from the photoexcitation of electrons from intra-bandgap trap states to the conduction band,[68,75] as illustrated in Figure S18 (Supporting Information). The significantly smaller magnitude of SPV under illumination for the NiFeOOH-containing samples suggests a decreased density of surface trap states. This is confirmed by the second illumination cycle increasing the difference in SPV magnitude even further. Such surface states located energetically close to the valence band edge (Figure 4g) act as hole traps, and their passivation by NiFeOOH is expected to improve hole transfer and reduce non-radiative recombination, thereby improving the photocurrent and the PEC device performance. As we inferred in a recent review,[11] passivating r-ss located at a high anodic potential is a highly efficient method for boosting water oxidation with $BiVO_4$.

2.4. Role of Bismuthene and NiFeOOH on Charge Transfer Kinetics

To better understand the interfacial charge transfer under illumination, photoelectrochemical impedance spectroscopy (PEIS) was conducted at a wide range of applied biases for all the prepared photoanodes. Nyquist plots show two semicircles with an offset from zero (**Figure 5**a,b). The offset is assigned to a series resistance (R_s) originating from the electrolyte, external circuit, and conductive substrate layer.[76] To identify the origin of the high-frequency > 10^3 Hz semicircle (the left one), PEIS measurements were compared among a Pt plate electrode, a bare FTO-coated glass, a thinner $BiVO_4$ photoanode (7 min deposition), and our standard $BiVO_4$ photoanode (17 min deposition). The high-frequency semicircle is not present in the Pt electrode; therefore, the high-frequency semicircle is not from the system components. The semicircle is already present in the bare FTO-coated glass, so they are related (Figure 5b). Its high frequency agrees with a fast carrier process, such as the expected fast charge transport at the FTO layer or charge transfer at the FTO/$BiVO_4$ interface. Moreover, the width of this high-frequency semicircle decreases for

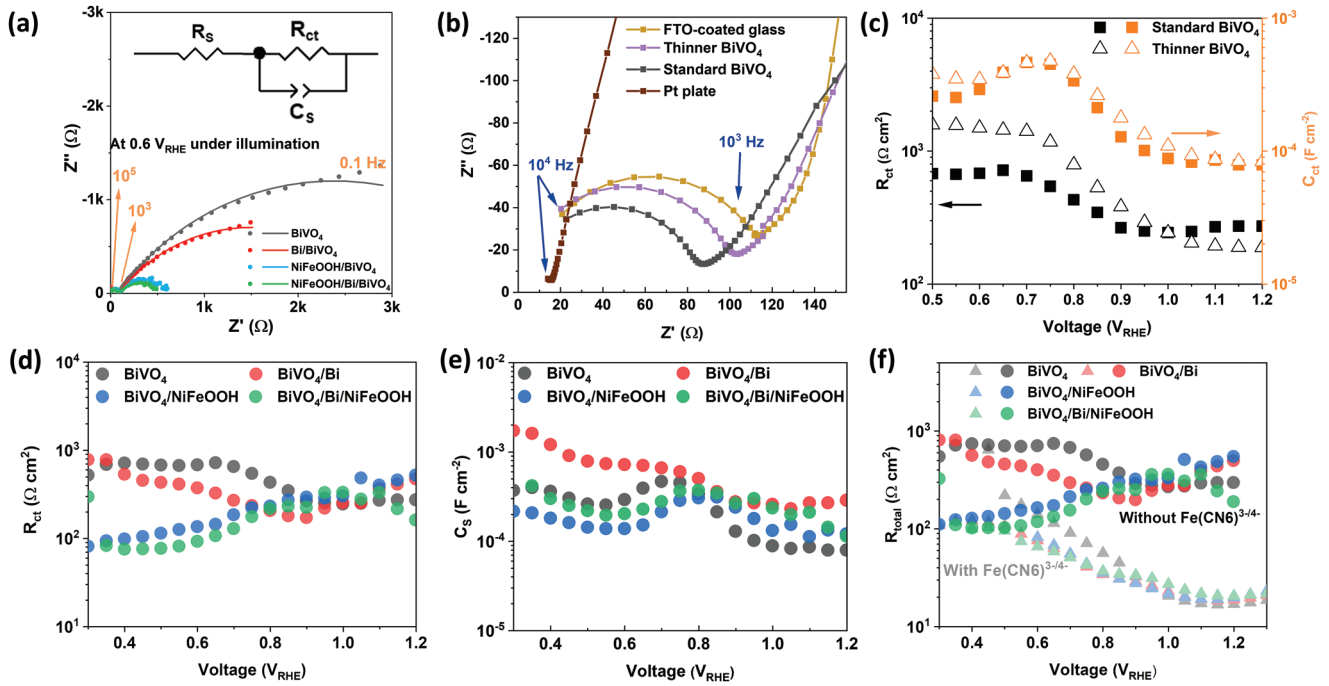

Figure 5. a) PEIS equivalent circuit and plots of $BiVO_4$ photoanodes in a 1 M KB buffer solution with pH 9 under simulated sunlight (Xe source, AM 1.5G, 100 mW cm^{-2}) at +0.6 V_{RHE} (dots represent PEIS experimental data whereas lines represent the fitting results); b,c) PEIS plots and fitting results of $BiVO_4$ photoanodes and a FTO-coated glass; d,e) Fitting results of R_{ct} and C_s as a function of applied potential; f) Fitting results of R_{total} of $BiVO_4$ photoanodes in a 1 M KB buffer solution with and without 100 mM $[Fe(CN)_6]^{3-/4-}$.

higher $BiVO_4$ coverage and thickness, in agreement with the expected decreased resistance between FTO and more $BiVO_4$ compared with that between FTO and electrolyte. Then, this high-frequency semicircle is assigned to the transport at the FTO substrate and is considered as part of the series resistance (R_s). Regarding the low-frequency 0.1–10^3 Hz semicircle (the right one), the comparison between our standard $BiVO_4$ photoanode and a thinner one shows a strong relation between its associated resistance element (R) value and the thickness—the thinner $BiVO_4$ photoanode has a resistance value one order of magnitude higher, so this resistance cannot be a bulk one, but one that depends on the surface area (Figure 5c).[77] Moreover, both the resistance and capacitance elements highly depend on the applied bias. Therefore, this low-frequency semicircle is assigned to charge transfer across the $BiVO_4$-electrolyte junction, defined by a resistance (R_{ct}) and a surface pseudo-capacitance (C_s) that scales down with applied bias.[77,78] The resulting equivalent model for these $BiVO_4$ photoanodes containing all the impedance elements is drawn in the inset of Figure 5a.

Nyquist plots at +0.6 V_{RHE} show smaller low-frequency semicircles for the bismuthene- and NiFeOOH-containing $BiVO_4$ photoanodes, indicating that these additives play an important role on boosting the interfacial charge transfer kinetics (Figure 5a). The analysis of Nyquist plots in the range +0.4–1.2 V_{RHE} shows that the R_{ct} of $BiVO_4$ without NiFeOOH significantly increases for a bias below +1 V_{RHE}, whereas the ones with NiFeOOH keep low values at any bias in agreement with the excellent catalytic activity of NiFeOOH (Figure 5d). The increase of R_{ct} indicates a cumbersome charge transfer between the bare $BiVO_4$ and the electrolyte and the necessity for co-catalysts. In addition to NiFeOOH, bismuthene also alleviates the R_{ct}, since there is a clear cathodic shift of the increase of R_{ct} from +1.00 V_{RHE} down to +0.75 V_{RHE}, the energy level of the oxygen vacancies. Such cathodic shift with bismuthene can be attributed to its catalytic activity (Figure S13a, Supporting Information) and improved electron extraction. We also observe that both NiFeOOH and bismuthene influence C_s (Figure 5e). NiFeOOH decreases C_s below +0.85 V_{RHE} and slightly shifts the peak at +0.7 V_{RHE}, whereas bismuthene increases C_s for any bias (Figure 5e). These C_s trends agree with our observations that NiFeOOH passivates hole-trap states whereas bismuthene increases the density of V_O. Nonetheless, as R_{ct} shows, bismuthene keeps filled these V_O-related shallow electron-trapping sites, thereby improving electron extraction.

To get further insights into the interfacial charge transfer, the PEIS measurements for OER were compared to those in the presence of a hole scavenger $[Fe(CN)_6]^{3-/4-}$. The total resistance (R_{total}) of the photoanodes with and without hole scavenger were calculated as $R_{total} = R_S + R_{ct}$ and plotted in Figure 5f.[79] Low R_{total} values are observed for any photoanode in the presence of the hole scavenger, but for PEC OER the R_{total} values are high, which validates that for OER the main contribution to the total resistance stems from the charge transfer step. The addition of bismuthene first and NiFeOOH afterward both drastically lower the R_{total} values, in agreement with their improved photocurrents and more cathodic potential onsets (Figure 5a). Further calculations were carried out comparing the photocurrents with and without Na_2SO_3 hole scavenger in the electrolyte, to calculate the charge injection efficiency, presented in Figure S19 (Supporting Information). In agreement with PEIS, charge injection efficiencies at different applied biases

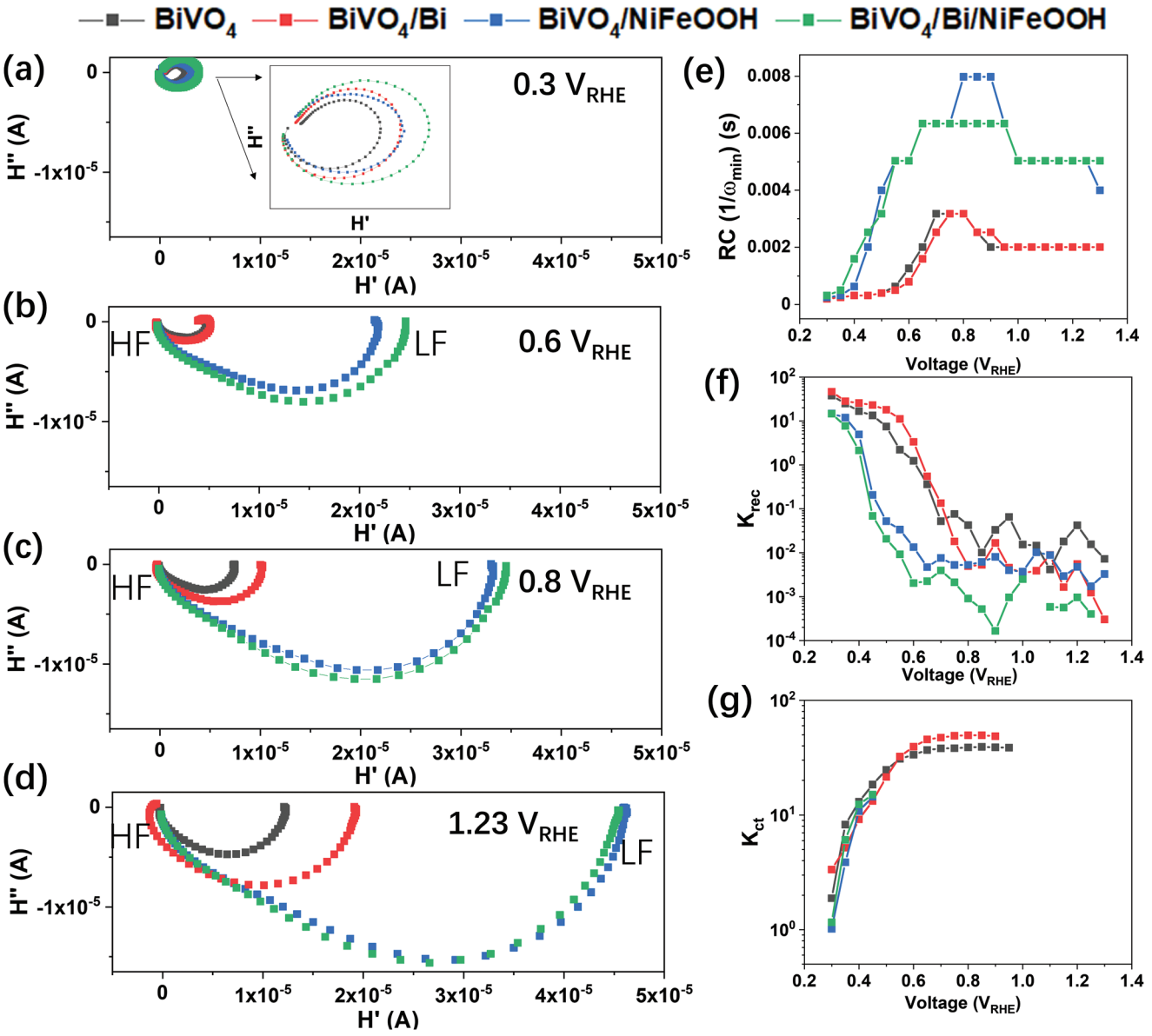

Figure 6. a–d) IMPS plots of $BiVO_4$ photoanodes measured in a 1 M KB buffer solution with pH 9 under different potential bias (The surface area of photoanodes is 0.28 cm^{-2}). e–g) Time constant RC (τ) and rate constants (k_{rec} and k_{ct}) calculated using IMPS plots at various potentials.

are superior with the addition of bismuthene and NiFeOOH, confirming that both improve charge transfer to the electrolyte.

Intensity-modulated photocurrent spectroscopy (IMPS) was conducted to investigate the surface kinetics related to rate constants for charge transfer (k_{ct}) and recombination (k_{rec}). The IMPS plots of the various photoanodes are shown in **Figure 6** and Figure S20 (Supporting Information). All the plots demonstrate depressed—rather than perfect—semicircles like those in the PEIS plots, an effect caused by the distributed time constants from porous and defective structures. At +0.3 V_{RHE} (the flat band potential), the low frequency intercepts (LFI) are located near the origin, indicating that almost all surface holes recombine, as expected. With the increase of applied bias, the plots change from two semicircles to one semicircle accompanied by increasing high frequency intercepts (HFI). This indicates that the anodic applied bias can result in reduced surface recombination and, therefore, increase the surface hole concentration.

At potentials below +0.8 V_{RHE}, k_{rec} decreases whereas k_{ct} increases with the increasing applied bias for all four photoanodes, both changes favoring the interfacial charge injection. The decrease of k_{rec} could be assigned to the development of band bending, whereas the increase of k_{ct} is caused by the activation of the catalytic reaction.[80] k_{ct} keeps similar values after loading bismuthene or NiFeOOH, indicating that both do not serve as catalysts in these potentials. This suggests that the charge transfer still occurs via the $BiVO_4$ surface.[80] k_{rec} decreases significantly after loading NiFeOOH, compared with that of bare $BiVO_4$. Since, the loading of NiFeOOH does not change OCP values (Figure 4b), band bending triggered by the

addition of NiFeOOH must has little impact on suppressing recombination in these potentials. An alternative explanation for the decrease in k_{rec} is that NiFeOOH passivates surface defects at that recombination occurs (r-ss).[80] k_{rec} of $BiVO_4$/Bi is similar to that of $BiVO_4$, indicating that bismuthene does not influence r-ss. These observations regarding r-ss agree with our SPV results.

At potentials above +0.8 V_{RHE}, k_{rec}, and k_{ct} keep constant (some values for k_{ct} beyond +0.5 V_{RHE} could not be identified clearly). This plateau and unavailable values result from the (nearly) invisible recombination semicircle (upper semicircle). The disappearance of the recombination semicircle indicates that almost all holes that reach the semiconductor surface are injected into the electrolyte.[1] It should be noticed that the photoanodes modified with both bismuthene and NiFeOOH have a significantly larger intercept with the x axis at higher frequencies (HFI) compared to bare $BiVO_4$, revealing that both bismuthene and NiFeOOH favor the hole flux to the surface. However, they have different influence on the time (τ) and rate (k_{rec} and k_{ct}) constants. First, the value of the time constant, τ, is hardly affected by the presence of bismuthene whereas it is significantly increased by the presence of NiFeOOH. This difference shows that it is mainly NiFeOOH increasing the hole lifetime, an observation consistent with the smaller anodic onset potential for NiFeOOH-containing photoanodes (Figure 3a). Second, the bismuthene-loaded photoanodes have slightly lower k_{rec} above +0.7 V_{RHE}, and the semicircle in the first quadrant decreased more dramatically compared to the bismuthene-free photoanodes. These features indicate a greater hole flux in bismuthene-loaded photoanodes and agree with the observed larger photovoltage in OCP tests (Figure 4b) and/or increased band bending in Kelvin probe measurements (Figure 4a). Finally, since some values for k_{ct} beyond +0.5 V_{RHE} could not be identified clearly, we cannot conclude whether the OER happens on $BiVO_4$ or Bi (and/or NiFeOOH) at the potential above +0.8 V_{RHE}. However, k_{ct} of $BiVO_4$/Bi is higher than that of bare $BiVO_4$, confirming a better charge injection, which probably results from the increased surface V_O concentration (if the OER happens on $BiVO_4$) or from the OER catalytic activity of Bi (if OER happens on Bi).

2.5. Discussion on Mechanism

Based on our characterization and tests, we propose the following mechanism for the improved interfacial charge transfer in the composite $BiVO_4$/Bi/NiFeOOH photoanodes (see energy diagram in **Figure 7**). Under illumination, $BiVO_4$ absorbs photons to generate electrons and holes. With the assistance of bias, electrons are extracted through the FTO-coated substrate, while holes are transferred toward the surface of $BiVO_4$ where two different surface states are present: 1) V_O related-surface states, that function as adsorption sites for the formation of oxy/hydroxyl-based water oxidation intermediates at the surface but also as shallow electron traps limiting charge extraction, and 2) VO^{2+}/VO_2^+ sites, that act as hole traps and recombination centers. The addition of a bismuthene functional layer generates an increased density of V_O as evidenced by XPS, and a significantly shallower Fermi level on the surface as measured by a Kelvin probe. This also means that bismuthene fills V_O-related shallow trap states with charges improving electron extraction in addition to a better developed, larger interfacial band bending helping charge separation. Moreover, the presence of VO^{2+}/VO_2^+ hole trap states in $BiVO_4$ can be successfully passivated by the addition of NiFeOOH: the holes accumulated on the surface are rapidly transferred and consumed as the NiFeOOH layer does not only enhance OER kinetics, but also passivates the recombination sites of VO^{2+}/VO_2^+. In summary, bismuthene and NiFeOOH can improve the interfacial hole injection by separately modulating the two different surface states. Moreover, the NiFeOOH layer can physically protect the bismuthene from peeling off.

3. Conclusion

In this work, a $BiVO_4$/bismuthene/NiFeOOH composite photoanode for photoelectrochemical water oxidation has been successfully constructed. The PEC performance is significantly improved by loading these two functional layers, a partially oxidized bismuthene and NiFeOOH, in this order. The optimized photocurrent density is 5.8 times higher compared

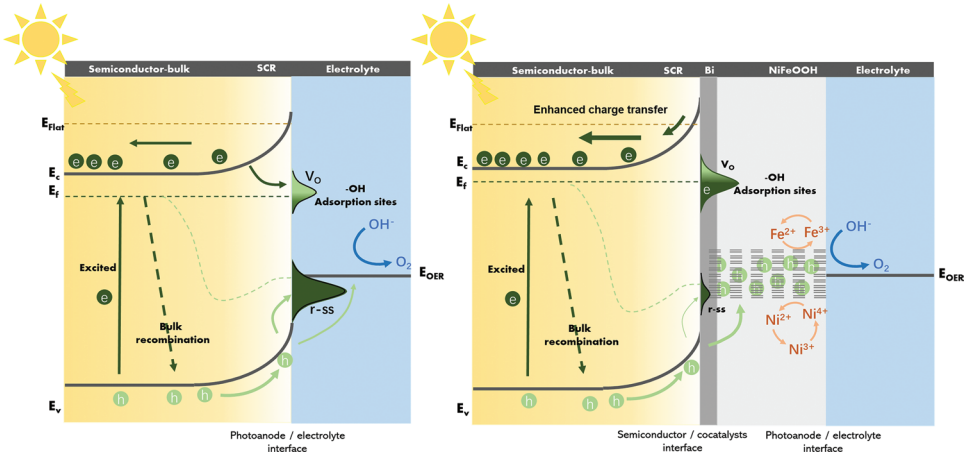

Figure 7. Schematic model showing the PEC processes on (left) bare $BiVO_4$ and (right) $BiVO_4$/Bi/NiFeOOH photoanodes Note: the thicknesses of the space charge region, bismuthene, and NiFeOOH are not to scale.

to bare $BiVO_4$ at +0.8 V_{RHE}, reaching an outstanding photocurrent of 3.4 (±0.2) mA cm^{-2} at this low bias of +0.8 V_{RHE}, or 4.7(±0.2) mA cm^{-2} at +1.23 V_{RHE}. A comprehensive analysis, including OCP, XPS, CV scan, LSV scan, PEIS, EIS, and IMPS, proves that there are two types of surface states on $BiVO_4$: V_O acting as shallow electron traps and VO^{2+}/VO_2^+ sites acting as hole traps; bismuthene and NiFeOOH modulate these two types of surface states in distinct ways. Bismuthene increases the density of V_O that are electron trap states but, keeping these states filled, electron extraction is enhanced as well as band bending for a better charge transport; whereas NiFeOOH passivates hole trap states decreasing surface recombination and boosting oxygen evolution. Through these effects, the synergistic cooperation of bismuthene and NiFeOOH significantly reduces surface recombination and enhances electron extraction and hole injection. We believe that these findings provide promising avenues to tune $BiVO_4$ photoanodes and inspire the design of novel photoanodes with functional interlayers implemented to attain a superior photoelectrochemical performance.

Supporting Information

Supporting Information is available from the Wiley Online Library or from the author.

Acknowledgements

S.E. and M.D. thank the EPSRC grant EP/S030727/1 for financial support. S.G. acknowledges the Ministerio de Economía y Competitividad (MINECO) from Spain (PID2020-116093RB-C41) and University Jaume I (UJI-B2019-20) for financial support.

Conflict of Interest

The authors declare no conflict of interest.

Data Availability Statement

The data that support the findings of this study are openly available in the Imperial College London research data repository at https://doi.org/10.14469/hpc/10930 reference number [81].

Keywords

2D bismuthene, $BiVO_4$ photoanodes, co-catalysts, oxygen vacancies, surface states

Received: June 23, 2022
Revised: July 29, 2022
Published online:

[1] L. Hans-Joachim, L. Peter, *Photoelectrochemical Water Splitting: Materials, Processes and Arhitectures*, RSC Publishing, London **2013**.
[2] H. C. Fu, P. Varadhan, C. H. Lin, J. H. He, *Nat. Commun.* **2020**, *11*, 3930.
[3] M. Ma, K. Zhang, P. Li, M. S. Jung, M. J. Jeong, J. H. Park, *Angew. Chemie* **2016**, *128*, 11998.
[4] A. Fujishima, H. Kenichi, *Nature* **1972**, *238*, 37.
[5] H. G. Yang, C. H. Sun, S. Z. Qiao, J. Zou, G. Liu, S. C. Smith, H. M. Cheng, G. Q. Lu, *Nature* **2008**, *453*, 638.
[6] J. Zhang, R. García-Rodríguez, P. Cameron, S. Eslava, *Energy Environ. Sci.* **2018**, *11*, 2972.
[7] T. W. Kim, K. S. Choi, *Science* **2014**, *343*, 990.
[8] H. S. Han, S. Shin, D. H. Kim, I. J. Park, J. S. Kim, P. S. Huang, J. K. Lee, I. S. Cho, X. Zheng, *Energy Environ. Sci.* **2018**, *11*, 1299.
[9] J. Eichhorn, C. Kastl, J. K. Cooper, D. Ziegler, A. M. Schwartzberg, I. D. Sharp, F. M. Toma, *Nat. Commun.* **2018**, *9*, 2597.
[10] D. K. Lee, D. Lee, M. A. Lumley, K. S. Choi, *Chem. Soc. Rev.* **2019**, *48*, 2126.
[11] J. Zhang, J. Cui, S. Eslava, *Adv. Energy Mater.* **2021**, *11*, 2003111.
[12] J. Li, X. Gao, Z. Li, J. H. Wang, L. Zhu, C. Yin, Y. Wang, X. B. Li, Z. Liu, J. Zhang, C. H. Tung, L. Z. Wu, *Adv. Funct. Mater.* **2019**, *29*, 1808079.
[13] X. Wang, K. H. Ye, X. Yu, J. Zhu, Y. Zhu, Y. Zhang, *J. Power Sources* **2018**, *391*, 34.
[14] Q. Bu, S. Li, K. Zhang, Y. Lin, D. Wang, X. Zou, T. Xie, A. C. S. Sustain, *Chem. Eng.* **2019**, *7*, 10971.
[15] C. Tang, B. Sun, M. Li, J. Zhang, X. Fan, F. Gao, Y. Tong, L. Dong, Y. Li, *J. Mater. Chem. A* **2019**, *7*, 8050.
[16] K. Zhang, B. Jin, C. Park, Y. Cho, X. Song, X. Shi, S. Zhang, W. Kim, H. Zeng, J. H. Park, *Nat. Commun.* **2019**, *10*, 2009.
[17] R. Gui, H. Jin, Y. Sun, X. Jiang, Z. Sun, *J. Mater. Chem. A* **2019**, *7*, 25712.
[18] F. Yang, A. O. Elnabawy, R. Schimmenti, P. Song, J. Wang, Z. Peng, S. Yao, R. Deng, S. Song, Y. Lin, M. Mavrikakis, W. Xu, *Nat. Commun.* **2020**, *11*, 1088.
[19] E. Aktürk, O. Uzengi Aktürk, S. Ciraci, *Phys. Rev. B* **2016**, *94*, 14115.
[20] F. Reis, G. Li, L. Dudy, M. Bauernfeind, S. Glass, W. Hanke, R. Thomale, J. Schäfer, R. Claessen, *Science* **2017**, *357*, 287.
[21] M. Pumera, Z. Sofer, *Adv. Mater.* **2017**, *29*, 1605299.
[22] P. Guo, X. Li, T. Feng, Y. Zhang, W. Xu, *ACS Appl. Mater. Interfaces* **2020**, *12*, 31757.
[23] C. Shen, T. Cheng, C. Liu, L. Huang, M. Cao, G. Song, D. Wang, B. Lu, J. Wang, C. Qin, X. Huang, P. Peng, X. Li, Y. Wu, *J. Mater. Chem. A* **2020**, *8*, 453.
[24] D. K. Lee, K. S. Choi, *Nat. Energy* **2018**, *3*, 53.
[25] A. Kudo, K. Omori, H. Kato, *J. Am. Chem. Soc.* **1999**, *121*, 11459.
[26] F. Yang, A. O. Elnabawy, R. Schimmenti, P. Song, J. Wang, Z. Peng, S. Yao, R. Deng, S. Song, Y. Lin, M. Mavrikakis, W. Xu, *Nat. Commun.* **2020**, *11*, 1088.
[27] B. Guo, S.-H. Wang, Z.-X. Wu, Z.-X. Wang, D.-H. Wang, H. Huang, F. Zhang, Y.-Q. Ge, H. Zhang, *Opt. Express* **2018**, *26*, 22750.
[28] T. Feng, X. Li, T. Chai, P. Guo, Y. Zhang, R. Liu, J. Liu, J. Lu, Y. Ge, *Beilstein Arch.* **2019**, 201928.
[29] L. Lu, Z. Liang, L. Wu, Y. Chen, Y. Song, S. C. Dhanabalan, J. S. Ponraj, B. Dong, Y. Xiang, F. Xing, D. Fan, H. Zhang, *Laser Photon. Rev.* **2018**, *12*, 1700221.
[30] A. Esparza-García, A. Reyes-Contreras, J. G. Bañuelos-Muñetón, M. Camacho-López, M. A. Camacho-López, O. Olea-Mejía, S. Camacho-López, *Opt. Mater. Express* **2017**, *7*, 1777.
[31] W. Zhang, Y. Hu, L. Ma, G. Zhu, P. Zhao, X. Xue, R. Chen, S. Yang, J. Ma, J. Liu, Z. Jin, *Nano Energy* **2018**, *53*, 808.
[32] H. Pei, Y. Wei, X. Guo, B. Wang, *Optik (Stuttg)* **2019**, *180*, 967.
[33] M. A. Zepeda, M. Picquart, E. Haro-Poniatowski, *MRS Proc.* **2012**, *1477*, 28.
[34] J. F. Moulder, W. F. Stickle, P. E. Sobol, K. D. Bomben, J. Chastain, Handbook of X-ray Photoelectron Spectroscopy: A Reference Book of Standard Spectra for Identification and Interpretation of XPS Data, Perkin-Elmer Corporation, **1992**.

[35] A. A. Kistanov, S. K. Khadiullin, K. Zhou, S. V. Dmitriev, E. A. Korznikova, *J. Mater. Chem. C* **2019**, *7*, 9195.
[36] R. Nyholm, A. Berndtsson, N. Mhrtensson, *J. Phys. C: Solid State Phys.* **1980**, *13*.
[37] M. Zhao, Y. Gu, W. Gao, P. Cui, H. Tang, X. Wei, H. Zhu, G. Li, S. Yan, X. Zhang, Z. Zou, *Appl. Catal. B Environ.* **2020**, *266*, 118625.
[38] S. Wang, T. He, J. H. Yun, Y. Hu, M. Xiao, A. Du, L. Wang, *Adv. Funct. Mater.* **2018**, *28*, 1802685.
[39] S. Tanuma, C. J. Powell, D. R. Penn, *Surf. Interface Anal.* **2011**, *43*, 689.
[40] I. Ohdomari, M. Oshima, A. Hiraki, Control of semiconductor interfaces: proceedings of the First International Symposium on Control of Semiconductor Interfaces, Karuizawa, Japan, 8–12 November **1993**.
[41] J. Pan, B. Wang, J. Wang, H. Ding, W. Zhou, X. Liu, J. Zhang, S. Shen, J. Guo, L. Chen, C. Au, L. Jiang, S. Yin, *Angew. Chem., Int. Ed.* **2021**, *60*, 1433.
[42] H. Idriss, *Surf. Sci.* **2021**, *712*, 121894.
[43] S. Selim, E. Pastor, M. García-Tecedor, M. R. Morris, L. Francàs, M. Sachs, B. Moss, S. Corby, C. A. Mesa, S. Gimenez, A. Kafizas, A. A. Bakulin, J. R. Durrant, *J. Am. Chem. Soc.* **2019**, *141*, 18791.
[44] A. R. Puigdollers, P. Schlexer, S. Tosoni, G. Pacchioni, *ACS Catal.* **2017**, *7*, 6493.
[45] D. Liu, C. Wang, Y. Yu, B. H. Zhao, W. Wang, Y. Du, B. Zhang, *Chem* **2019**, *5*, 376.
[46] L. Hao, K. Miyazawa, H. Yoshida, Y. Lu, *Mater. Res. Bull.* **2017**, *97*, 13.
[47] S. Yu, Y. Zhang, F. Dong, M. Li, T. Zhang, H. Huang, *Appl. Catal. B Environ.* **2018**, *226*, 441.
[48] Y. Ma, A. Kafizas, S. R. Pendlebury, F. L.e Formal, J. R. Durrant, *Adv. Funct. Mater.* **2016**, *26*, 4951.
[49] M. N. Shaddad, P. Arunachalam, A. A. Alothman, A. M. Beagan, M. N. Alshalwi, A. M. Al-Mayouf, *J. Catal.* **2019**, *371*, 10.
[50] Y. Gao, G. Yang, Y. Dai, X. Li, J. Gao, N. Li, P. Qiu, L. Ge, *ACS Appl. Mater. Interfaces* **2020**, *12*, 17364.
[51] Y. Zhang, Y. Li, D. Ni, Z. Chen, X. Wang, Y. Bu, J. P. Ao, *Adv. Funct. Mater.* **2019**, *29*, 1902101.
[52] J. H. Kim, J. S. Lee, *Adv. Mater.* **2019**, *31*, 1806938.
[53] Z. Y. Wu, W. B. Ji, B. C. Hu, H. W. Liang, X. X. Xu, Z. L. Yu, B. Y. Li, S. H. Yu, *Nano Energy* **2018**, *51*, 286.
[54] H. Han, K. M. Kim, H. Choi, G. Ali, K. Y. Chung, Y. R. Hong, J. Choi, J. Kwon, S. W. Lee, J. W. Lee, J. H. Ryu, T. Song, S. Mhin, *ACS Catal.* **2018**, *8*, 4091.
[55] S. Gao, Y. Lin, X. Jiao, Y. Sun, Q. Luo, W. Zhang, D. Li, J. Yang, Y. Xie, *Nat. 2016 5297584* **2016**, *529*, 68.
[56] B. Ni, P. He, W. Liao, S. Chen, L. Gu, Y. Gong, K. Wang, J. Zhuang, L. Song, G. Zhou, X. Wang, E. B. Ni, K. Wang, J. Zhuang, X. Wang, P. He, W. Liao, G. Zhou, S. Chen, L. Song, L. Gu, Y. Gong, *Small* **2018**, *14*, 1703749.
[57] S. Yan, W. Liao, M. Zhong, W. Li, C. Wang, N. Pinna, W. Chen, X. Lu, *Appl. Catal. B Environ.* **2022**, *307*, 121199.
[58] K. Liu, F. Wang, P. He, T. A. Shifa, Z. Wang, Z. Cheng, X. Zhan, J. He, K. Liu, F. M. Wang, P. He, T. A. Shifa, Z. Wang, Z. Cheng, X. Zhan, J. He, *Adv. Energy Mater.* **2018**, *8*, 1703290.
[59] S. Zhang, I. Ahmet, S. Kim, O. Kasian, A. M. Mingers, P. Schnell, M. Ko, J. Lim, A. Fischer, K. J. J. Mayrhofer, S. Cherevko, B. Gault, R. Van De Krol, C. Scheu, *ACS Appl. Energy Mater.* **2020**, *3*, 9523.
[60] F. M. Toma, J. K. Cooper, V. Kunzelmann, M. T. McDowell, J. Yu, D. M. Larson, N. J. Borys, C. Abelyan, J. W. Beeman, K. M. Yu, J. Yang, L. Chen, M. R. Shaner, J. Spurgeon, F. A. Houle, K. A. Persson, I. D. Sharp, *Nat. Commun.* **2016**, *7*, 12012.
[61] R. T. Gao, L. Wu, S. Liu, K. Hu, X. Liu, J. Zhang, L. Wang, *J. Mater. Chem. A* **2021**, *9*, 6298.
[62] B. J. Trześniewski, W. A. Smith, *J. Mater. Chem. A* **2016**, *4*, 2919.
[63] E. Y. Liu, J. E. Thorne, Y. He, D. Wang, *ACS Appl. Mater. Interfaces* **2017**, *9*, 22083.
[64] N. J. Firet, A. Venugopal, M. A. Blommaert, C. Cavallari, C. J. Sahle, A. Longo, W. A. Smith, *Chem. Mater.* **2019**, *31*, 7453.
[65] K. Zhang, J. Liu, L. Wang, B. Jin, X. Yang, S. Zhang, J. H. Park, *J. Am. Chem. Soc.* **2020**, *142*, 8641.
[66] X. Yao, X. Zhao, J. Hu, H. Xie, D. Wang, X. Cao, Z. Zhang, Y. Huang, Z. Chen, T. Sritharan, *iScience* **2019**, *19*, 976.
[67] J. Hu, W. Chen, X. Zhao, H. Su, Z. Chen, *ACS Appl. Mater. Interfaces* **2018**, *10*, 5475.
[68] L. Kronik, Y. Shapira, *Surf. Sci. Rep.* **1999**, *37*, 1.
[69] M. Zhong, T. Hisatomi, Y. Kuang, J. Zhao, M. Liu, A. Iwase, Q. Jia, H. Nishiyama, T. Minegishi, M. Nakabayashi, N. Shibata, R. Niishiro, C. Katayama, H. Shibano, M. Katayama, A. Kudo, T. Yamada, K. Domen, *J. Am. Chem. Soc.* **2015**, *137*, 5053.
[70] A. Hankin, F. E. Bedoya-Lora, J. C. Alexander, A. Regoutz, G. H. Kelsall, *J. Mater. Chem. A* **2019**, *7*, 26162.
[71] A. J. Bard, A. B. Bocarsly, F. R. F. Fan, E. G. Walton, M. S. Wrighton, *J. Am. Chem. Soc.* **2002**, *102*, 3671.
[72] B. J. Trześniewski, I. A. Digdaya, T. Nagaki, S. Ravishankar, I. Herraiz-Cardona, D. A. Vermaas, A. Longo, S. Gimenez, W. A. Smith, *Energy Environ. Sci.* **2017**, *10*, 1517.
[73] Q. Shi, S. Murcia-López, P. Tang, C. Flox, J. R. Morante, Z. Bian, H. Wang, T. Andreu, *ACS Catal.* **2018**, *8*, 3331.
[74] J. B. Allen, L. R. Faulkner, *Electrochemical Methods: Fundamentals and Applications*, 2nd ed., Wiley, Weinheim, Germany **2010**.
[75] J. Luke, L. Corrêa, J. Rodrigues, J. Martins, M. Daboczi, D. Bagnis, J.-S. Kim, *Adv. Energy Mater.* **2021**, *11*, 2003405.
[76] J. Guan, J. Zhang, T. Yu, G. Xue, X. Yu, Z. Tang, Y. Wei, J. Yang, Z. Li, Z. Zou, *RSC Adv.* **2012**, *2*, 7708.
[77] S. Gimenez, H. K. Dunn, P. Rodenas, F. Fabregat-Santiago, S. G. Miralles, E. M. Barea, R. Trevisan, A. Guerrero, J. Bisquert, *J. Electroanal. Chem.* **2012**, *668*, 119.
[78] C. Choi, D. S. Ashby, D. M. Butts, R. H. DeBlock, Q. Wei, J. Lau, B. Dunn, *Nat. Rev. Mater.* **2019**, *5*, 5.
[79] B. Klahr, S. Gimenez, F. Fabregat-Santiago, J. Bisquert, T. W. Hamann, *Energy Environ. Sci.* **2012**, *5*, 7626.
[80] C. Zachäus, F. F. Abdi, L. M. Peter, R. Van De Krol, *Chem. Sci.* **2017**, *8*, 3712.
[81] Junyi Cui, 2022; Data for Two-Dimensional Bismuthene as a Functional Interlayer between $BiVO_4$ and NiFeOOH for Enhanced Oxygen-Evolution Photoanodes; Imperial College London Research Data Repository; 10.14469/hpc/10930 Metadata.